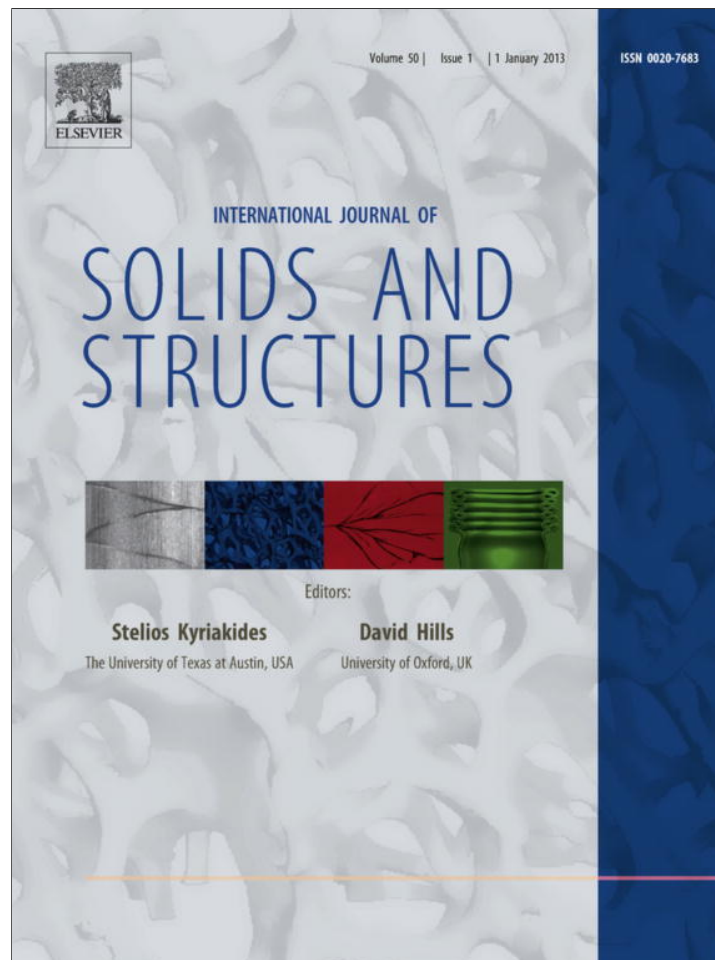


Provided for non-commercial research and education use.  
Not for reproduction, distribution or commercial use.



This article appeared in a journal published by Elsevier. The attached copy is furnished to the author for internal non-commercial research and education use, including for instruction at the authors institution and sharing with colleagues.

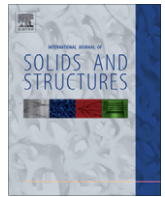
Other uses, including reproduction and distribution, or selling or licensing copies, or posting to personal, institutional or third party websites are prohibited.

In most cases authors are permitted to post their version of the article (e.g. in Word or Tex form) to their personal website or institutional repository. Authors requiring further information regarding Elsevier's archiving and manuscript policies are encouraged to visit:

<http://www.elsevier.com/copyright>

Contents lists available at [SciVerse ScienceDirect](http://www.sciencedirect.com)

## International Journal of Solids and Structures

journal homepage: [www.elsevier.com/locate/ijsolstr](http://www.elsevier.com/locate/ijsolstr)

## Disclination densities from EBSD orientation mapping

Benoît Beausir\*, Claude Fressengeas

Laboratoire d'Etude des Microstructures et de Mécanique des Matériaux (LEM3), Université de Lorraine/CNRS, Ile du Saulcy, 57045 Metz Cedex, France

## ARTICLE INFO

## Article history:

Received 14 September 2011  
 Received in revised form 7 September 2012  
 Available online 10 October 2012

## Keywords:

EBSD  
 Grain-boundaries  
 Triple junctions  
 Dislocations  
 Disclinations  
 GND

## ABSTRACT

The aim of the paper is to show experimental evidence of the rotational defects referred to as disclinations in polycrystalline aggregates. Using orientation maps obtained from electron backscattered diffraction or transmission electron microscopy, a method for the recovery of components of the disclination density tensor is presented and applied to various polycrystalline materials. Mapping the disclination densities reveals their extensive presence at intra-granular low-angle boundaries, low and high-angle grain boundaries and triple junctions, irrespective of the material symmetry and grain size. A significant level of rotational incompatibility, with dipolar distribution of the disclinations, is detected in all cases investigated. Since high-angle rotational incompatibility cannot be accounted for consistently by dislocation-based models, the present results support considering disclinations in addition to dislocations in the interpretation of grain boundaries and triple junctions.

© 2012 Elsevier Ltd. All rights reserved.

## 1. Introduction

Disclinations and dislocations are crystal defects simultaneously introduced by Volterra at the turn of the last century (Volterra, 1907). Dislocations arise from translational incompatibility of the crystal lattice, whereas disclinations originate in its rotational incompatibility (deWit, 1970, 1973). Disclinations have long been considered as secondary topics in the theory of crystal defect fields, perhaps because their occurrence as isolated crystal-line objects is precluded by the large level of elastic energy they involve, as compared with dislocations (Friedel, 1964). However self-screened disclination configurations, such as disclination dipoles, involve energy levels comparable to dislocation ensembles (Romanov and Vladimirov, 1992; Romanov and Kolesnikova, 2009). Being rotational defects, disclinations are *a priori* well suited for the description of imperfect lattice structures in instances, such as grain boundaries, where a single-valued elastic rotation field does not exist. Despite this predisposition, grain boundary modeling has preferentially used dislocation-based approaches over the last decades, most probably because low-angle boundaries have been directly observed to contain dislocation structures. Thus, employing the Frank–Bilby surface-dislocation concept (Frank, 1950; Bilby, 1955), dislocation-based models have become widely accepted for the description of low-angle boundaries. There may also be utility in modeling high-angle boundaries using a dislocation-based approach, although direct microscopic evidence of such dislocation structures is then lacking. Such models are efficient at

predicting geometrical properties of grain boundaries, such as the coupling factor relating the normal motion of a tilt boundary occurring in response to imposed shear (Cahn et al., 2006). However, boundaries terminating at triple junctions, the most frequent situation in polycrystals, cannot be portrayed consistently in this manner. Furthermore, accounting for high disorientation angles with a dislocation-based approach requires such large surface-dislocation densities that overlapping of dislocation cores may occur. For example, describing a 60° symmetric tilt-boundary with edge surface-dislocations needs a density of four dislocations per nm according to Frank's formula, a density overly in excess. Disclination-based models remove these limitations and cover more of the microscopic observations. They can be used to model high-angle boundaries and to account for their structure (Li, 1972; Shih and Li, 1975; Gertsman et al., 1989; Hurtado et al., 1995). Hence, experimental observation and quantitative characterization of disclinations through their density fields is of great interest.

Disclinations have indeed been inferred at grain boundaries from optical microscopy observations (Romanov and Kolesnikova, 2009), or observed in the grain interior using high-resolution transmission-electron-microscopy (Murayama et al., 2002; Motylenko et al., 2004). However, a situation similar to that described above in grain boundary modeling has been prevailing in electron backscattered diffraction (EBSD) investigations. Although the orientation maps contain information on rotational incompatibility, they have been used almost exclusively for the recovery of Nye's dislocation densities (El-Dasher et al., 2003; Field et al., 2005; Pantleon, 2008). Disclination densities have only recently been evidenced at triple junctions and low-angle boundaries (Zisman et al., 2008). The characterization of the dislocation densities from

\* Corresponding author.

E-mail address: [benoit.beausir@univ-lorraine.fr](mailto:benoit.beausir@univ-lorraine.fr) (B. Beausir).

orientation maps is based on a relationship established in the theory of crystal defect fields between the elastic curvature tensor, Nye's curvature tensor and the curl of the elastic strain tensor (deWit, 1970). Most often this last term is disregarded for the sake of simplicity, and the elastic curvature obtained from the orientation maps is equated with Nye's curvature. In the theory of dislocations, the elastic curvature tensor is defined as the gradient of the elastic rotation vector (Kröner, 1958, 1980). As such it is curl-free. However, if rotational incompatibility is present, it is not a gradient tensor anymore, and its curl yields a non-zero disclination density tensor (deWit, 1970).

In the present paper, we present a method using orientation maps to determine at least three components of the disclination density tensor. The objective is to help decide whether or not a theory of crystal defects involving disclinations in addition to dislocations is needed in a particular physical situation. The outline of the paper is as follows. In Section 2, after notation conventions are settled, we briefly review the theory of incompatibility in crystal-line solids (deWit, 1970), to provide a fundamental basis for the forthcoming Sections. Section 3 details the method for recovering components of the disclination tensor, and provides information on the particular materials investigated in this work. In Section 4, the corresponding maps of disclination densities are presented, together with a statistical analysis of their distribution. A discussion of these results is provided in Section 5, and conclusions follow.

## 2. Review of the incompatible elasto-static defect theory

Our notations are as follows. A bold symbol denotes a tensor. When there may be ambiguity, an arrow is superposed to represent a vector:  $\vec{\mathbf{V}}$ . The symbol  $\mathbf{A}\mathbf{B}$  represents multiplication of the tensors  $\mathbf{A}$  and  $\mathbf{B}$ , e.g.,  $(\mathbf{A}\mathbf{B})_{ij} = A_{ik}B_{kj}$  for second order tensors.  $\mathbf{A} \cdot \mathbf{B}$  represents the inner product of the two second order tensors  $\mathbf{A} : \mathbf{B} = A_{ij}B_{ij}$ , in rectangular Cartesian components, or the product of a higher order tensor with a second order tensor, e.g.,  $\mathbf{A} : \mathbf{B} = A_{ijkl}B_{kl}$ . The **div** and **curl** operations for second-order tensors are defined row by row, in analogy with the vectorial case. For any base vector  $\mathbf{e}_i$  of the reference frame:

$$(\mathbf{div} \mathbf{A})^t \cdot \mathbf{e}_i = \mathbf{div}(\mathbf{A}^t \cdot \mathbf{e}_i), \quad (1)$$

$$(\mathbf{curl} \mathbf{A})^t \cdot \mathbf{e}_i = \mathbf{curl}(\mathbf{A}^t \cdot \mathbf{e}_i). \quad (2)$$

In rectangular Cartesian components:

$$(\mathbf{div} \mathbf{A})_i = A_{ij,j}, \quad (3)$$

$$(\mathbf{curl} \mathbf{A})_{ij} = e_{jkl}A_{il,k}, \quad (4)$$

where  $e_{jkl}$  is a component of the third-order alternating Levi-Civita tensor  $\mathbf{X}$ , and a subscript comma indicates partial spatial differentiation. A vector  $\vec{\mathbf{A}}$  is associated with tensor  $\mathbf{A}$  by using its inner product with tensor  $\mathbf{X}$ :

$$(\vec{\mathbf{A}})_k = -\frac{1}{2}(\mathbf{A} : \mathbf{X})_k = -\frac{1}{2}e_{ijk}A_{ij}. \quad (5)$$

In the present framework, it is assumed that the displacement vector  $\mathbf{u}$  can be defined continuously at any point of a simply-connected body containing crystal defects. Therefore, the total distortion tensor defined as  $\mathbf{U} = \mathbf{grad} \mathbf{u}$  is curl-free:

$$\mathbf{curl} \mathbf{U} = 0. \quad (6)$$

Eq. (6) is a necessary condition for the integrability of the displacement  $\mathbf{u}$ . Conversely, this equation is sufficient to assure the existence of a single-valued continuous solution  $\mathbf{u}$  to the equation  $\mathbf{U} = \mathbf{grad} \mathbf{u}$ , up to a constant translation. Eq. (6) is referred to as the compatibility condition for the distortion  $\mathbf{U}$ . Defining the strain

tensor  $\boldsymbol{\epsilon}$  as the symmetric part of  $\mathbf{U}$ , the rotation tensor  $\boldsymbol{\omega}$  as its skew-symmetric part and the associated rotation vector  $\vec{\boldsymbol{\omega}}$  as:

$$\vec{\boldsymbol{\omega}} = -\frac{1}{2}\boldsymbol{\omega} : \mathbf{X}, \quad (7)$$

Eq. (6) becomes:

$$\mathbf{curl} \boldsymbol{\epsilon} + \mathbf{curl} \boldsymbol{\omega} = \mathbf{curl} \boldsymbol{\epsilon} + \mathbf{div}(\vec{\boldsymbol{\omega}})\mathbf{I} - \mathbf{grad}^t \vec{\boldsymbol{\omega}} = 0, \quad (8)$$

where  $\mathbf{I}$  is the identity tensor. Transposing, then taking the **curl** of Eq. (8) leads to:

$$\mathbf{curl} \mathbf{curl}^t \boldsymbol{\epsilon} = 0. \quad (9)$$

This relation is the well-known Saint-Venant compatibility condition for the strain  $\boldsymbol{\epsilon}$ . It is a necessary condition for the integrability of the displacement  $\mathbf{u}$ . The trace of Eq. (8) similarly yields a compatibility condition for the rotation vector in the form:

$$\mathbf{div}(\vec{\boldsymbol{\omega}}) = 0. \quad (10)$$

In the presence of dislocations, the elastic distortion  $\mathbf{U}_e$  contains a non-gradient incompatible part,  $\mathbf{U}_e^\perp$ , because the elastic displacement is not single-valued. A curl-free elastic compatible component,  $\mathbf{U}_e^\parallel$ , may also exist to satisfy the balance of equilibrium and boundary conditions, and the following relations are therefore satisfied:

$$\mathbf{U}_e = \mathbf{U}_e^\perp + \mathbf{U}_e^\parallel, \quad (11)$$

$$\mathbf{curl} \mathbf{U}_e^\perp = \boldsymbol{\alpha}, \quad (12)$$

where  $\boldsymbol{\alpha}$  may be non-zero. The incompatibility Eq. (12) defines the incompatible elastic distortion  $\mathbf{U}_e^\perp$  associated with the presence of Nye's dislocation density tensor  $\boldsymbol{\alpha}$ . Since  $\mathbf{U}_e^\parallel$  is curl-free, Eq. (12) is still true when  $\mathbf{U}_e^\perp$  is replaced with  $\mathbf{U}_e$ :

$$\mathbf{curl} \mathbf{U}_e = \boldsymbol{\alpha}. \quad (13)$$

Therefore, to ensure that the incompatible part  $\mathbf{U}_e^\perp$  vanishes identically throughout the body when  $\boldsymbol{\alpha} = 0$ , Eq. (12) must be augmented with the side conditions  $\mathbf{div} \mathbf{U}_e^\perp = \mathbf{0}$  and  $\mathbf{U}_e^\perp \cdot \mathbf{n} = \mathbf{0}$  on the boundary with unit normal  $\mathbf{n}$ . Further, the continuity condition:

$$\mathbf{div} \boldsymbol{\alpha} = 0 \quad (14)$$

follows directly from Eqs. (12) and (13).

Applying the above curl-trace procedure to the elastic distortion and Eq. (13), we obtain from the curl operation, with self-evident notations, an equation parallel to Eq. (8):

$$\mathbf{curl} \boldsymbol{\epsilon}_e + \mathbf{curl} \boldsymbol{\omega}_e = \mathbf{curl} \boldsymbol{\epsilon}_e + \mathbf{div}(\vec{\boldsymbol{\omega}}_e)\mathbf{I} - \mathbf{grad}^t \vec{\boldsymbol{\omega}}_e = \boldsymbol{\alpha}. \quad (15)$$

From the trace operation, we find an equation parallel to Eq. (10):

$$\mathbf{div}(\vec{\boldsymbol{\omega}}_e) = \frac{1}{2}\mathbf{tr}(\boldsymbol{\alpha}). \quad (16)$$

Motivated by the Saint-Venant compatibility condition (9), we transpose Eq. (15) and further rearrange with the help of Eq. (16), to obtain:

$$\mathbf{grad} \vec{\boldsymbol{\omega}}_e = \mathbf{curl}^t \boldsymbol{\epsilon}_e + \mathbf{K}, \quad (17)$$

$$\mathbf{K} = \frac{1}{2}\mathbf{tr}(\boldsymbol{\alpha})\mathbf{I} - \boldsymbol{\alpha}^t. \quad (18)$$

At this point, we can define the elastic curvature tensor,  $\boldsymbol{\kappa}_e$ , as:

$$\boldsymbol{\kappa}_e = \mathbf{grad} \vec{\boldsymbol{\omega}}_e \quad (19)$$

and take the **curl** of Eq. (17), to find:

$$\mathbf{curl} \boldsymbol{\kappa}_e = \mathbf{curl}(\mathbf{curl}^t \boldsymbol{\epsilon}_e + \mathbf{K}) = 0. \quad (20)$$

Hence, in the theory of dislocations, the elastic curvature tensor  $\boldsymbol{\kappa}_e$  is curl-free and an integrable quantity.  $\mathbf{K}$  is defined as Nye's

curvature tensor (Nye, 1953). Interestingly,  $\kappa_e$  can be directly measured from the orientation maps obtained by EBSD. By additionally recovering the elastic strain field to compute  $\mathbf{curl} \epsilon_e$ , one can experimentally infer the dislocation density tensor  $\alpha$  from Eqs. (17) and (18). Such information may be obtained from the analysis of the shift of electron diffraction patterns (Wilkinson et al., 2006; Kacher et al., 2009; Villert et al., 2009), but most often the  $\mathbf{curl} \epsilon_e$  term is overlooked and  $\kappa_e$  is equated with  $\mathbf{K}$  (El-Dasher et al., 2003; Field et al., 2005; Pantleon, 2008), which yields components of Nye's tensor  $\alpha$  through:

$$\alpha = \text{tr}(\mathbf{K})\mathbf{I} - \mathbf{K}^t, \quad (21)$$

a relationship reciprocal to Eq. (18), or through:

$$\alpha = \mathbf{curl} \omega_e. \quad (22)$$

If  $\kappa_e$  is not supposed to be curl-free anymore, i.e., if the possibility of its non-integrability and of a rotational incompatibility are acknowledged, then the rotation tensor  $\omega_e$  and rotation vector  $\vec{\omega}_e$  do not exist, and a non-zero tensor  $\theta$  such that

$$\theta = \mathbf{curl} \kappa_e \quad (23)$$

must be defined.  $\theta$  is the disclination density tensor, and Eq. (23) is part of the theory of crystal defects (dislocations and disclinations). It replaces Eq. (20), which pertains to the theory of dislocations. Eq. (23) implies that the elastic curvature tensor is not integrable and the elastic rotation not single-valued when the disclination density is non-zero. An incompatible elastic curvature,  $\kappa_e^\perp$ , is therefore associated with the presence of the disclination density  $\theta$ . A curl-free compatible part of the elastic curvature,  $\kappa_e^\parallel$ , may also exist in order to verify equilibrium equations and boundary conditions. As already discussed in the case of translational incompatibility, to ensure that the incompatible part  $\kappa_e^\perp$  vanishes identically throughout the body when  $\theta = 0$ , Eq. (23) must be replaced with:

$$\theta = \mathbf{curl} \kappa_e^\perp, \quad (24)$$

augmented with the side conditions  $\mathbf{div} \kappa_e^\perp = 0$  and  $\kappa_e^\perp \cdot \mathbf{n} = \mathbf{0}$  on the boundary with unit normal  $\mathbf{n}$ . These conditions ensure uniqueness of the solution. Eq. (23) shall be used in the next Section to determine disclination densities from orientation maps. The continuity condition for disclinations:

$$\mathbf{div} \theta = 0 \quad (25)$$

follows directly from Eqs. (23) and (24). It implies that disclination lines do not end inside the body. Since the rotation vector  $\vec{\omega}_e$  does not exist in the theory of crystal defects, the corresponding elastic distortion tensor  $\mathbf{U}_e$  is also undefined. Substituting the elastic curvature tensor  $\kappa_e$ , which now includes an incompatible part, for  $\mathbf{grad} \vec{\omega}_e$  in Eq. (15), leads to the modified equation:

$$\mathbf{curl} \epsilon_e = \alpha + \kappa_e^t - \text{tr}(\kappa_e)\mathbf{I}. \quad (26)$$

Eq. (26) defines the incompatible elastic strain associated with the dislocation density tensor  $\alpha$  in the concurrent presence of incompatible elastic curvature. The continuity condition (14) for dislocations is also modified in the theory of crystal defects. Taking the divergence of Eq. (26) and defining the twist-disclination vector  $\vec{\Theta}$  as:

$$\vec{\Theta} = -\frac{1}{2}\theta : \mathbf{X}, \quad (27)$$

it is found that:

$$\mathbf{div} \alpha + 2\vec{\Theta} = 0. \quad (28)$$

This continuity equation implies the existence of geometric interactions between twist-disclinations ( $i \neq j$ ) and dislocations. Its meaning is that dislocation lines can end on disclinations in the body. Of

course, when the disclination density vanishes, Eqs. (26) and (28) reduce to Eqs. (13) and (14), and the elastic theory of crystal defects reduces to the theory of dislocations. In the presence of orientation maps obtained from a polycrystalline material, the aim of the present paper is to give indications on whether a theory of crystal defects (dislocations and disclinations) or a theory of dislocations is suitable for an interpretation.

### 3. Method and experiments

By means of conventional EBSD or any other technique of orientation mapping, local lattice orientations are known at individual points in a regular grid on a planar surface of a sample. Let us use a square grid, aligned with the unit vectors ( $\mathbf{e}_1, \mathbf{e}_2$ ) of the sample reference frame ( $\mathbf{e}_1, \mathbf{e}_2, \mathbf{e}_3$ ), and denote the components of the elastic rotation vector  $\vec{\omega}_e$  as: ( $\theta_i; \forall i \in (1, 2, 3)$ ). The disorientation vector between two neighboring points A and B is  $\Delta\theta\mathbf{r} = \Delta\theta_i\mathbf{e}_i$ , where  $\Delta\theta$  denotes the disorientation angle and  $\mathbf{r}$  the disorientation axis. It derives from the rotation mapping one local lattice frame onto the other, or from the disorientation tensor  $\Delta\mathbf{g} = \mathbf{g}_A^{-1} \cdot \mathbf{g}_B$  where the orientation tensors ( $\mathbf{g}_A, \mathbf{g}_B$ ) specifying the rotation of the lattice at both locations are composed. The analysis readily shows that the components  $\Delta\theta_i$  of the disorientation vector are  $\Delta\theta_i = \mathbf{e}_{ijk}\Delta\mathbf{g}_{jk}\Delta\theta/2\sin(\Delta\theta)$  (Pantleon, 2008). From the disorientations  $\Delta\theta_i$  between neighboring points separated with  $\Delta x_i$ , only six components of the elastic curvature tensor can be captured, because differences along the normal direction  $\mathbf{e}_3$  are not available:

$$\kappa_{il}^e \approx \frac{\Delta\theta_i}{\Delta x_l}; \quad \forall i \in (1, 2, 3), \quad \forall l \in (1, 2). \quad (29)$$

Using this result, it was shown from Eq. (21) that five dislocation densities can be recovered, namely: ( $\alpha_{12}, \alpha_{13}, \alpha_{21}, \alpha_{23}, \alpha_{33}$ ) in the present reference frame (Pantleon, 2008). In the absence of disclinations, Eq. (22) was alternatively used to recover the dislocation densities (see for example (El-Dasher et al., 2003; Pantleon, 2008)), because the components  $\omega_{ij}^e$  of the elastic rotation matrix can be approximated as  $\omega_{ij}^e \approx g_{ij} - \delta_{ij}$  for small disorientations, with help of the orientation matrix components  $g_{ij}$ . Consequently, the dislocation density tensor, as provided by Eq. (22), may be written in terms of the orientation tensor  $\mathbf{g}$  as:

$$\alpha = \mathbf{curl} \mathbf{g} \quad (30)$$

with identical conclusions. However, Eq. (30) is invalidated in the presence of disclinations, because the elastic rotation tensor does not exist anymore. The recovery of disclination densities involves differences in the elastic curvatures. In component form, Eq. (23) reads:

$$\theta_{ij} = \mathbf{e}_{jkl}\kappa_{il,k}^e \quad (31)$$

Hence, it is readily seen from Eqs. (29) and (31) that the three components:  $\theta_{i3}, \forall i \in (1, 2, 3)$  are directly obtained from conventional planar measurements. In contrast with the recovery of dislocation densities, no additional information on the elastic strain field is needed in this determination process. A complete recovery of the nine disclination densities can follow if the differences in the orientation angles and curvatures become available in the third direction  $\mathbf{e}_3$ . Such information can be obtained by carefully erasing thin slices orthogonal to  $\mathbf{e}_3$ , by using for example the focused ion beam technology.

The grain boundaries and triple junctions were defined as follows from the orientation maps. First, the disorientation of each pixel with its four (north, south, east and west) neighbors was examined. When the disorientation exceeded the "grain tolerance angle" (here 5°), a boundary was defined. Note that, as a consequence, grain boundaries coincide with pixel boundaries. Once

**Table 1**  
Orientation and topographic data in the analyzed samples.

Material	History	Average diameter ( $\mu\text{m}$ )	Nb. of grains	Nb. of triple junctions	$3^\circ < \theta \leq 5^\circ$ (%)	$5^\circ < \theta \leq 15^\circ$ (%)
Copper	ECAP 1 pass	0.79	1187	1592	40.57	37.79
Aluminum	Electrodeposited	0.028	3160	4989	1.06	5.72
IF-steel	ECAP 3 passes	0.309	712	844	47.72	24.59
Titanium	Annealed, 1% tension	4.00	3738	7122	0.22	3.64

the set of all boundaries was captured, a flood-fill procedure was applied to search for sub-areas bounded by a closed boundary. Such sub-areas were defined as grains. A triple junction was acknowledged when three different grains were detected in a  $2 \times 2$  pixels array. Quadruple junctions were also obtained, but they are not studied *per se* in this work. Table 1 includes the main disorientation and connection features found in this way in all samples analyzed in the present work. The grain average diameter given in the third column was obtained by using the equivalent circle area method. As can be seen from the number of grains and triple junctions, the statistical sampling was sufficient in all samples. The fractions of boundaries in the ranges  $3^\circ$ – $5^\circ$  and  $5^\circ$ – $15^\circ$  are also given in the table for all samples investigated. In the present state of the art, the angular accuracy of orientation mapping by EBSD is about  $0.5^\circ$ . In the experiments reported in the present paper, the spatial resolution was in the range 6.5 nm through  $0.2 \mu\text{m}$ , and the spatial accuracy was about 1 nm. In such conditions, Eq. (31) shows that the disclination densities at grain boundaries are inferred with a 20% error for  $5^\circ$  disorientations, but that the relative error may reduce to about 1% when the disorientation reaches the highest angles, e.g.,  $90^\circ$  in hcp materials. Therefore, confidence in the results acquired for low-angle boundaries is limited, but the orientation properties of high-angle boundaries should be rendered rather properly. The five available components of the dislocation density tensor were acquired by using the analysis detailed in Pantleon (2008). With the angular and spatial resolution indicated above, the relative error in their measurement ranges from about 1% to 10%.

The analysis, *i.e.* the determination of the dislocation and disclination density fields, was first applied to fcc materials subjected to equal channel angular pressing (ECAP) at room temperature. It has been suggested that disclination-based approaches could help explain the peculiarities of the flow stress dependence on the grain size in nano-grained materials (Romanov and Vladimirov, 1992; Romanov and Kolesnikova, 2009). Evidencing the presence of disclinations in ECAPed materials would support these ideas. The disclination maps shown in Fig. 1 were extracted from OFHC copper deformed by one pass leading to the average shear strain  $\gamma = 2$ . The EBSD measurements were carried out at Monash University by SEM on a LEO 1530 FEG instrument with a step size of  $0.2 \mu\text{m}$ . Automated orientation analyses of the Kikuchi patterns were performed using the Channel 5 software package produced by HKL Technology. The mapping was performed in the plane of normal ND (see Fig. 1). Detailed description of the experimental procedure can be found in Tóth et al. (2010). In contrast, the orientation map in Fig. 2 was obtained from a sub-micron aluminum thin self-standing film produced by electrodeposition technique (see (Malhaire et al., 2009) for details). The measurements were performed at the Institut National Polytechnique in Grenoble (SIMaP laboratory) using a Transmission Electron Microscope (TEM) equipped with the SPINNING STAR technology produced by NanoMEGAS. Orientation mapping on a grid with a 6.5 nm step was carried out by analyzing the diffraction patterns with the ASTAR package.

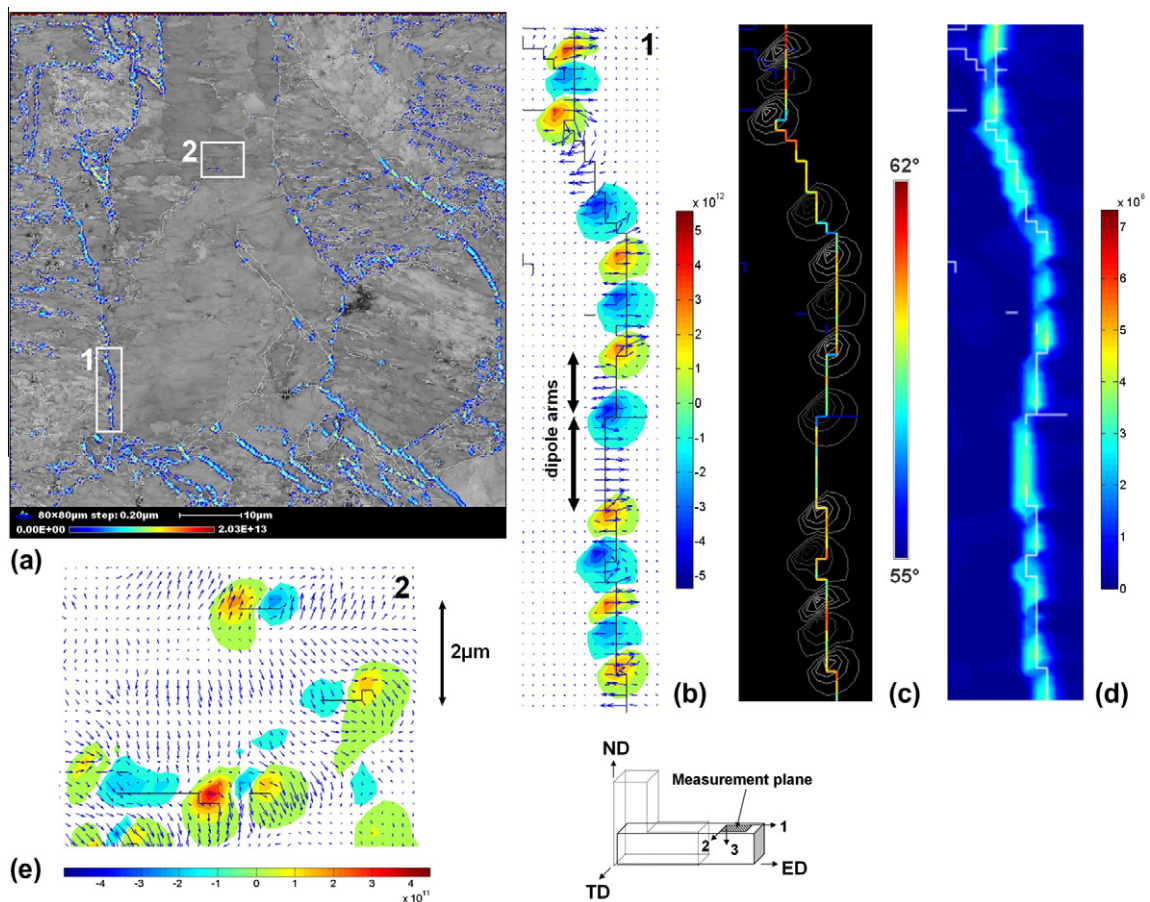
The analysis was similarly applied to bcc and hcp materials. The orientation map in Fig. 3 was extracted from an IF-Steel submitted to ECAP, after three passes in route Bc at  $300^\circ\text{C}$ , leading to an

average shear strain  $\gamma = 6$ . The measurements were performed at the Indian Institute of Science (Bangalore), using a FEI-SIRION field emission gun scanning electron microscope (FEG-SEM). The map was obtained in the plane of normal TD (see Fig. 3). More details can be found in Beausir et al. (2009). Finally, we used a technically pure titanium in  $\alpha$  phase, fully statically recrystallized at  $720^\circ\text{C}$ . Figs. 4 and 5 were obtained after 1% strain in tension. The EBSD measurements were performed at Université de Lorraine (LEM3-Metz) using a FEG-SEM. The orientations were mapped using the Channel 5 software package, with a  $0.2 \mu\text{m}$  step size. Note that the close-up map shown in Fig. 4 includes only 1% of the full scanned area ( $295 \times 218 \mu\text{m}^2$ ). Since the data were very extensive, statistical analysis of the maps was also conducted. The results, shown in Fig. 5, will be discussed below.

#### 4. Results

All the samples investigated involve widespread presence of large disclination densities at low-angle sub-grain boundaries, low-angle and high-angle grain boundaries, and triple junctions, irrespective of the lattice structure, grain size and strain level. In Figs. 1–4, the disclination densities are displayed in color-code, using either the scalar measure  $\theta = \sqrt{\theta_{13}^2 + \theta_{23}^2 + \theta_{33}^2}$ , which involves all measured disclination densities, or the wedge density  $\theta_{33}$ . The arrows show the Burgers vector  $\mathbf{b}$  associated with the edge-dislocation densities  $(\alpha_{13}, \alpha_{23})$  per unit-surface:  $\mathbf{b} = \alpha_{13}\mathbf{e}_1 + \alpha_{23}\mathbf{e}_2$ . Fig. 1(d) additionally shows the length  $\sqrt{\alpha_{13}^2 + \alpha_{23}^2}$  of this vector using a contour map. The corresponding dislocation line is collinear with  $\mathbf{e}_3$ , the unit vector normal to the figure. The density of disclinations in grain boundaries ranges from  $5 \times 10^{12} \text{ rad m}^{-2}$  in ECAPed copper (Fig. 1) to  $5 \times 10^{15} \text{ rad m}^{-2}$  in the as deposited aluminum thin film (Fig. 2). It is usually orders of magnitude lower in the bulk of the crystals, where it can be comparatively neglected. A visual inspection of the grain boundaries can be conducted in the subsets (b) in Figs. 1–3, where blow-ups of several grain boundaries are shown, and in Fig. 4. The pixel size ranges from 6.5 nm in Fig. 2 through  $0.2 \mu\text{m}$  in Fig. 1. At such resolution length scales, the disclinations are seen as extended objects characterized by an aerial density, typically spreading over  $20 \times 20 \text{ nm}^2$  in Fig. 2 and  $2 \mu\text{m}^2$  in Fig. 4. The observation reveals disclination dipoles aligned along the grain boundaries, as a positive wedge-disclination area can systematically be coupled up with a close negative wedge area. Thus, the dipoles build linear arrays of alternatively positive and negative wedge disclinations  $\theta_{33}$ . As a rule of thumb, a wedge-disclination dipole features in its interior a distribution of edge dislocations  $(\alpha_{13}, \alpha_{23})$  whose Burgers vector is approximately normal to the dipole arm (see Fig. 1(b)).<sup>1</sup> Quadrupoles can also be observed (see Fig. 4). Typically, the dipole separation is of the order of 10 nm in

<sup>1</sup> It is perhaps useful to recall here that dislocation densities collectively refer to ensembles of dislocation lines threading pixel-size patches (6.6 nm through 200 nm in the present investigation). Note that the number of involved dislocations may be rather small at the smallest pixel size.



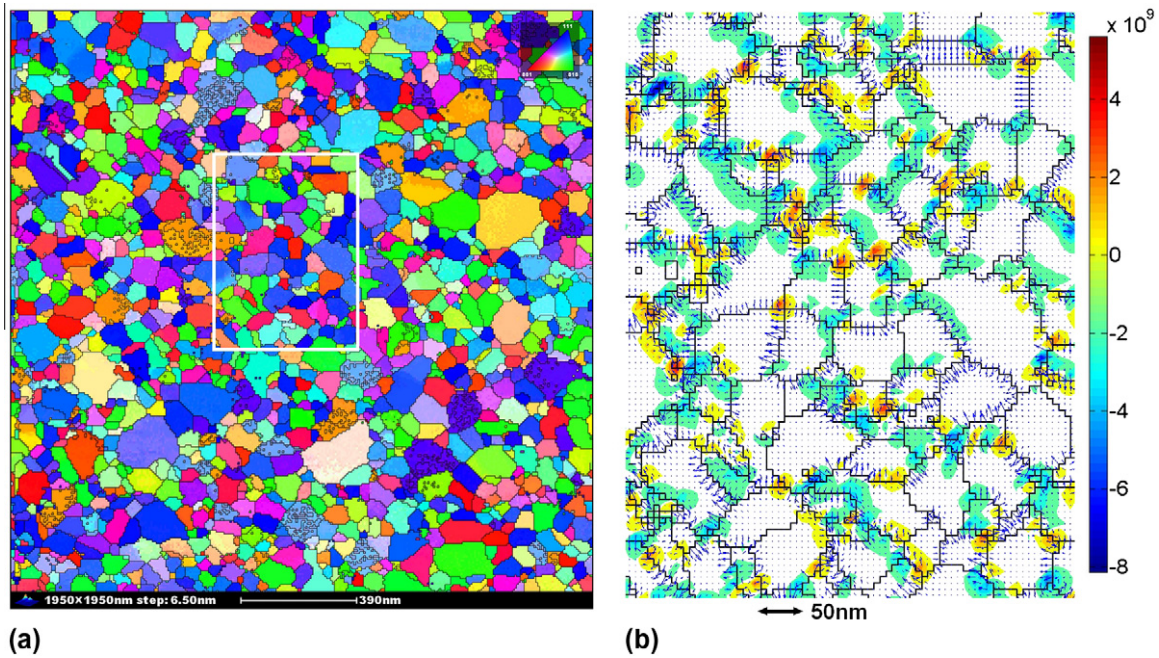
**Fig. 1.** Pure copper ECAPed, one pass. Shear strain  $\gamma = 2$ . The main map (a) represents the scalar disclination measure  $\theta = \sqrt{\theta_{13}^2 + \theta_{23}^2 + \theta_{33}^2}$  in  $\text{rad m}^{-2}$ . The close-up maps (b), (c) and (d) show respectively the density of wedge disclinations  $\theta_{33}$  (in  $\text{rad m}^{-2}$ ), the disorientation and the scalar dislocation measure  $\sqrt{\alpha_{13}^2 + \alpha_{23}^2}$  in  $\text{m}^{-1}$  (i.e. the length of the local Burgers vector per unit surface resulting from the dislocation densities  $(\alpha_{13}, \alpha_{23})$ ) along a high-angle boundary, while the close-up map (e) shows  $\theta_{33}$  (in  $\text{rad m}^{-2}$ ) along low angle sub-grain boundaries. In the subsets (b,e), the arrows represent the local Burgers vectors: their horizontal and vertical components are respectively  $\alpha_{13}$  and  $\alpha_{23}$  (in  $\text{m}^{-1}$ ). The maximum Burgers vector length corresponds to a  $3.85 \times 10^6 \text{ m}^{-1}$  dislocation density. A continuous line indicates the presence of a disorientation of at least  $5^\circ$ . The disorientation lies in the range  $55^\circ$ – $62^\circ$  along the grain boundary shown in subsets (b,c,d). The black arrows in subset (b) highlight two successive dipoles with vertical arm lengths, horizontal Burgers vectors (normal to the arm length) and inverse polarities. Note the inversion of the Burgers vectors direction in the dipoles interiors.

Fig. 2 and  $1 \mu\text{m}$  in Fig. 1. The edge dislocations are in relation with the grains disorientation along the boundary, while the disclination dipoles correlate with the variations in this disorientation (compare Fig. 1(b) and (c)). It may sometimes look rather periodic, but is most often irregular. Intra-granular disclination dipoles associated with sub-grain boundaries can also be seen in Fig. 1(e). The presence of rotational incompatibility in the neighborhood of triple junctions is frequently observed in Figs. 1–4, but a close disclination area of opposite sign may not be immediately available for dipole pinpointing. Nevertheless, the dipolar structure of the set of triple junctions is recovered in a statistical sense. Indeed, Fig. 5 presents the probability  $P(\theta_{33})$  of occurrence of the wedge disclinations  $\theta_{33}$  in the complete titanium data set, a small 1% subset of which was used to build Fig. 4. Using our *EBSDFmcf* software (Beausir and Fundenberger, xxxx) for the analysis of orientation maps, two different disclination sets were considered in building this figure: (i) the complete set including all boundaries and triple junctions, (ii) the subset involving only triple junctions. Low-angle boundary data were discarded in this figure to avoid inaccuracy at small wedge densities. Note in Table 1 that 7122 triple junctions were detected in the entire map. A  $4 \times 4$  pixels array was considered around each triple junction to define its disclination content. It is seen that all distributions are fully symmetric with respect to zero-wedge density, which statistically proves dipolar status. Symmetric statistical distributions were similarly obtained in all other cases investigated in this paper. In

addition, plotting  $P(\theta_{33})$  in logarithmic scales shows that it obeys a power law  $P(\theta_{33}) \sim \theta_{33}^{-n}$  over an order of magnitude, with  $n \approx 1.4$  and  $n \approx 1.5$  for triple junctions only and all grain boundaries respectively. The cutoff seen at large disclination densities takes place because a maximum misorientation between grains is existing, which eliminates the possibility of an exponential dependence.

### 5. Discussion

In this Section, we discuss the structure of a disclination dipole, as well as the alternating dipole sequences dotting the grain boundaries and the triple junctions evidenced in Figs. 1–4. As already mentioned, disclination dipoles are self-screened configurations whose elastic energy level compares to that of dislocation ensembles. Thus, the dipolar character of the observed disclination distributions is reassuring regarding their plausibility. In the elastic theory of crystal defects (dislocations and disclinations), disclination dipoles are defined as a close pair of discrete line-disclinations of opposite sign (de Wit, 1973). In the present work, they are rather described as a close pair of extended areas supporting disclination densities of opposite sign. This continuous rather than singular point of view is motivated in the first place by the finiteness of the pixel size. However, it also reflects the widespread occurrence of large disclination densities over several contiguous pixels. Further, arrays of edge dislocations are observed inside the wedge



**Fig. 2.** As-deposited aluminum thin film. Map (a) shows the inverse pole figure. The close-up map (b) shows the density of wedge disclinations  $\theta_{33}$  in  $\text{rad m}^{-2}$ . The arrows represent the local Burgers vector resulting from the dislocation densities ( $\alpha_{13}, \alpha_{23}$ ): their horizontal and vertical components are respectively  $\alpha_{13}$  and  $\alpha_{23}$  (in  $\text{m}^{-1}$ ). The maximum Burgers vector length corresponds to a  $1.20 \times 10^8 \text{ m}^{-1}$  dislocation density. A continuous line indicates the presence of a disorientation of at least  $5^\circ$ . Note the direction of the Burgers vector, often normal to the dipole arm.

disclination dipoles, with in-plane Burgers vector normal to the dipole arm. The sense of the Burgers vector in the array is in relation with the polarity of the dipole, as can be seen from two consecutive dipoles in the midst of Fig. 1(b). An alternating arrangement of disclination dipoles along grain boundaries has been predicted by the Disclination Structural Units models (DSU) for grain boundaries (Li, 1972; Shih and Li, 1975; Gertsman et al., 1989). However, our observations are qualitatively and quantitatively different. First, DSU models are based on singular rather than continuous disclination dipoles. Second, the separation distance of the dipoles amounts to nanometers in the DSU models, whereas the presently observed dipoles reflect variations in the curvature over tens to hundreds of nms. Indeed the curvature variations at nm scale remain unresolved in the present work, due to an exceedingly large pixel size. However, this observation raises questions as to how such dipolar structures at different scales might relate to each other.

Like grain boundaries, triple junctions and their properties can be addressed from the use of disclinations. Two critical issues are that of their energy (Fortier et al., 1991; Srinivasan et al., 1999; Nazarov et al., 2003) and of their dislocation/disclination character (Bollmann, 1991; Dimitrakopoulos et al., 1996). In incompatible polycrystals, triple junctions may have disclination and/or dislocation character if surface-dislocations and surface-disclinations are allowed to accommodate tangential discontinuities of the elastic strain and curvature tensors along the abutting grain boundaries (Dimitrakopoulos et al., 1996; Upadhyay et al., 2011; Fressengeas et al., 2012). Instead, compatibility of the polycrystal results in the balance of the Burgers or Frank vector at triple junctions. In this case, no disclination and/or dislocation character is assigned to triple junctions. In this Frank–Bilby-type point of view, grain boundaries are seen as interfaces with no width and triple junctions as discrete lines. If, in contrast with such a singular approach, continuous modeling of the grain boundaries is adopted in the sense that tangential continuity of the elastic strain and curvature tensors is required and recourse to singular surface-dislocation and

surface-disclination densities is dismissed, then all grain boundaries have a width and all triple junctions are dislocation/disclination free (Upadhyay et al., 2011; Fressengeas et al., 2012). Whether or not a triple junction has dislocation/disclination character in a Frank–Bilby perspective cannot be decided on the basis of the present results because, as already mentioned, the pixels do not embody a boundary in our orientation maps. Instead, the present observations are consistent with a continuous point of view, inasmuch as rotational incompatibility is not assigned to the boundaries and triple junctions but to their close surroundings.

In addition to a visual inspection of Figs. 1–4, the dipolar structure of the disclinations in our samples is self-obvious from the probability  $P(\theta_{33})$  of occurrence of the wedge-disclination density  $\theta_{33}$  shown in Fig. 5. Indeed, it is fully symmetric with respect to the sign of  $\theta_{33}$ . The symmetry holds not only for the set of all grain boundaries in the orientation map, but also for the subset composed of triple junctions only. The symmetry in disclination density probability bears witness to the overall balance over the map of rotational incompatibility and of the associated internal stresses and couple-stresses. As seen in Fig. 6, decreasing the size of the map does not prevent symmetry to hold, except in much smaller samples. Only subsets including less than about 30 grains, such as the subset shown in Fig. 4, lead to non-symmetric probability. This feature is indicative of a critical sample size below which residual stresses become unbalanced. In the present case, an estimate of the latter is  $20 \mu\text{m}$ , i.e. about the height of Fig. 4. Note also in Fig. 5 that the fraction of rotational incompatibility that can be assigned to triple junctions increases with the disclination density level. High rotational incompatibility values are therefore preferentially localized in triple junctions. As mentioned in Section 4, plotting  $P(\theta_{33})$  in logarithmic scales shows that it obeys a power law  $P(\theta_{33}) \sim \theta_{33}^{-n}$  over an order of magnitude. A power-law relationship is indication of the self-similarity of the dependency: regardless of the value of the density, the same scaling exponent  $n$  describes the asymptotic behavior of the probability. Moreover, if the probability satisfies the above power law, it also obeys the

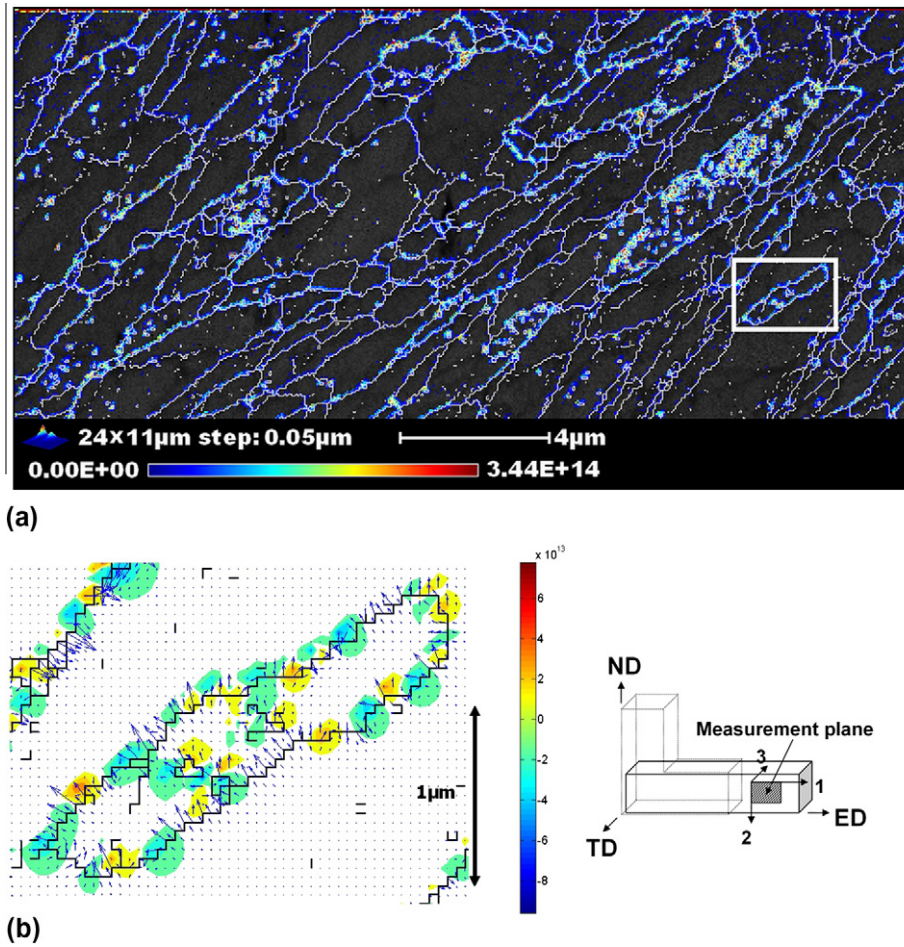


**Fig. 3.** IF-steel ECAPed, one pass. Shear strain  $\gamma = 6$ . The main map represents the scalar disclination measure  $\theta = \sqrt{\theta_{13}^2 + \theta_{23}^2 + \theta_{33}^2}$  (in  $\text{rad m}^{-2}$ ). The inset map shows a close-up of the wedge disclination density  $\theta_{33}$  along a grain boundary (in  $\text{rad m}^{-2}$ ). The arrows represent the local Burgers vectors resulting from the dislocation densities  $(\alpha_{13}, \alpha_{23})$ , whose horizontal and vertical components are respectively  $\alpha_{13}$  and  $\alpha_{23}$  (in  $\text{m}^{-1}$ ). The maximum Burgers vector length corresponds to a  $1.57 \times 10^7 \text{ m}^{-1}$  dislocation density.

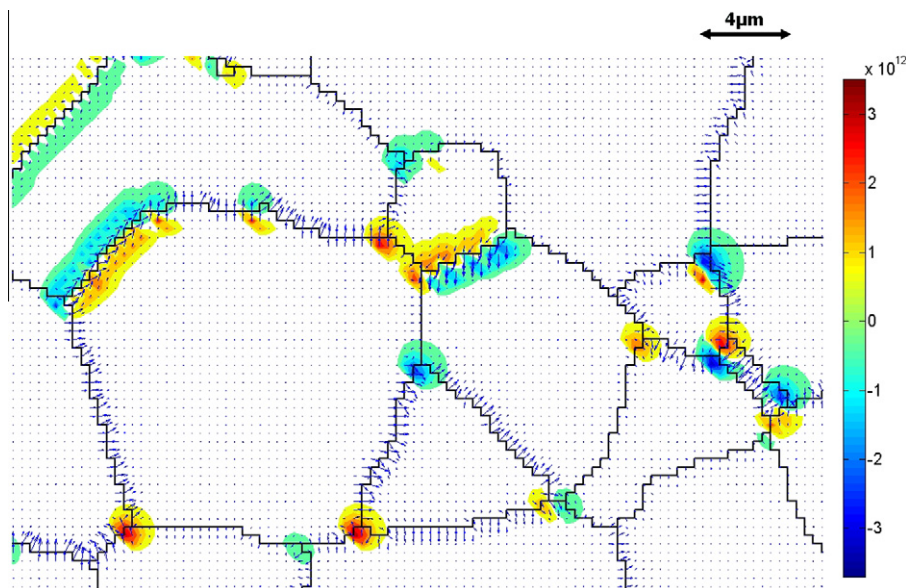


**Fig. 4.** Recrystallized titanium, 1% strain, density of wedge disclinations  $\theta_{33}$  (in  $\text{rad m}^{-2}$ ). The arrows represent the Burgers vector resulting from the dislocation densities  $(\alpha_{13}, \alpha_{23})$  ( $\alpha_{13}$  and  $\alpha_{23}$  are the horizontal and vertical components respectively, in  $\text{m}^{-1}$ ). The maximum Burgers vector length corresponds to a  $5.19 \times 10^6 \text{ m}^{-1}$  dislocation density. The step size is  $0.2 \mu\text{m}$ . Note the quadrupole to the right of the figure.

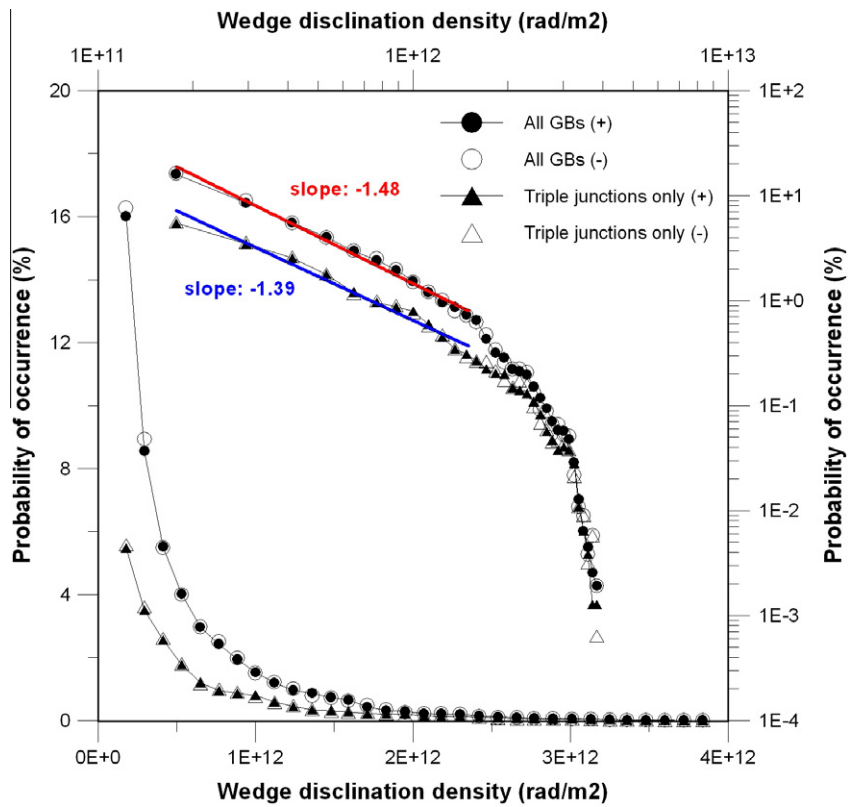


Fig. 5. Probability of occurrence of positive (+) vs. negative (-) wedge disclination density  $\theta_{33}$  (in  $\text{rad m}^{-2}$ ) in the titanium data set (a 1% subset is shown in Fig. 4). Full circles: all positive wedges; open circles: all negative wedges; full triangles: positive triple junction wedges; open triangles: negative triple junction wedges. The same data are shown in linear scales (bottom and left) and logarithmic scales (top and right).

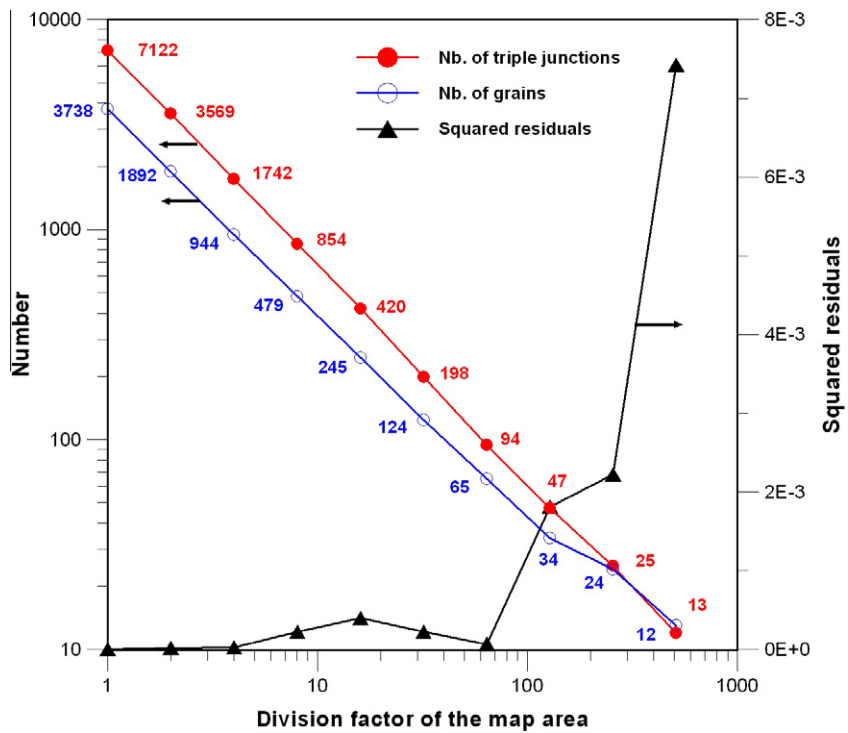


Fig. 6. Squared residuals between positive and negative wedge densities  $\theta_{33}$  vs. map reduction factor (triangles). The open and full circles indicate the numbers of grains and triple junctions in the reduced map. The grains and triple junctions of a map downsized by a factor  $n$  are all included in the map reduced at the order  $(n - 1)$  ( $n \geq 2$ ).

functional equation  $P(k\theta_{33}) \sim k^{-n}P(\theta_{33})$  (and vice versa). This scaling symmetry implies that no characteristic density is involved in the dependence of the probability. Thus, the power-law relationship suggests scale-invariant spatial correlations between areas featuring rotational incompatibility. A reasonable conjecture is that these correlations originate in the long-distance stresses and couple-stresses associated with the presence of dislocations and disclinations along grain boundaries. Since the scaling exponent is smaller than average for triple junctions, the correlations of the latter decrease less quickly in space. The scale invariance is preserved with the same scaling exponent when the sample area is reduced by a factor 64, which suggests, consistent with the above conjecture, that spatial correlations due to internal stresses and couple-stresses are still present in much smaller samples.

## 6. Conclusion

With notable pioneering exceptions, the role of disclinations in the description of imperfect crystal lattices has probably been underestimated in the past decades, whether from a modeling or an experimental point of view. The present recovery of rotational incompatibility from experimental orientation maps suggests that the elastic theory of crystal defects, which features disclinations in addition to dislocations, may be useful for a consistent account of the network of grain boundaries constitutive of a polycrystal. Indeed, widespread presence of disclinations at grain boundaries and triple junctions was found in all materials investigated in the present work, irrespective of the crystal symmetry, grain size and loading history. Complex crystal defects combining extended disclination dipoles with dislocation arrays were evidenced. These dislocation/disclination structures align and form alternating sequences along grain boundaries, as suggested by disclination-based structural units models at a smaller scale.

Only a third of all disclination densities were determined in the present investigation, due to the planar character of our orientation maps. We believe that although they would allow a much more detailed description of the grain boundaries, fully volumetric maps would not fundamentally contradict the present observations and conclusions. Indeed, any complementary (yet unknown) disclination density would add to the presently measured rotational incompatibility. It is also very likely that the remaining disclination densities would be found mainly along grain boundaries, and would feature a self-screened distribution of dipoles. Even in their present incomplete state, our observations are pleading for the additional involvement of disclinations in an elastic theory of grain boundaries and triple junctions.

The present observations are also a motivation for a dynamic theory of elasto-plasticity accounting for both dislocations and disclinations (Fressengeas et al., 2011, 2012). The contribution of disclinations to plasticity can perhaps be ignored in coarse-grained polycrystals, where dislocation-mediated plasticity models are offering widely accepted descriptions. However, dislocation mechanisms cannot be invoked anymore in nano-grained polycrystals, where grain boundary mechanisms are good candidates for an alternative description of plasticity. Migration of grain boundaries, grain rotation about grain boundaries, reactions at triple junctions and dislocation emission/absorption by grain boundaries are mechanisms that have been proposed in this aim. Their understanding may benefit from a description in the framework of a dynamic elasto-plastic theory of dislocations and disclinations.

## Acknowledgments

The authors gratefully acknowledge Chengfan F. Gu (Department of Materials Engineering, Monash University, Clayton,

Australia), Nilesh P. Guroo (Department of Materials Engineering, Indian Institute of Science, Bangalore, India), Sabine Lay and Edgar F. Rauch (Laboratoire de Science et Ingénierie des Matériaux et des Procédés, Institut National Polytechnique/CNRS, Grenoble, France), Nicolas Bayona and Francis Wagner (Laboratoire d'Etude des Microstructures et de Mécanique des Matériaux, Université de Lorraine/CNRS, France), who kindly provided the orientation maps in copper, IF-steel, aluminum and titanium, respectively.

## References

- Beausir, B., Fressengeas, C., Guroo, N.P., Tóth, L.S., Suwas, S., 2009. Spatial correlation in grain misorientation distribution. *Acta Mater.* 57, 5382–5395.
- Beausir, B., Fundenberger, J., 2010. Software for orientation image mapping. <<http://benoitbeausir.free.fr>>.
- Bilby, B.A., 1955. Types of dislocation source. In: Bristol Conference Report on Defects in Crystalline Solids, The Physical Society, London, vol. 124.
- Bollmann, W., 1991. The stress field of a model triple-line disclination. *Mat. Sci. Eng. A* 136, 1–7.
- Cahn, J.W., Mishin, Y., Suzuki, A., 2006. Coupling grain boundary motion to shear deformation. *Acta Mater.* 54, 4953–4975.
- de Wit, R., 1970. Linear theory of static disclinations. In: Simmons, J.A., de Wit, R., Bullough, R. (Eds.), *Fundamental Aspects of Dislocation Theory*, NBS Spec. Publ. (National Bureau of Standards), Washington, DC, vol. 317, no. 1, pp. 651–680.
- de Wit, R., 1973. Theory of disclinations: IV. Straight disclinations. *J. Res. Natl. Bureau Stand. – A Phys. Chem.* 77A, 607–658.
- Dimitrakopoulos, G.P., Karakostas, Th., Pond, R.C., 1996. The defect character of interface junction lines. *Interf. Sci.* 4, 129–138.
- El-Dasher, B.S., Adams, B.L., Rollett, A.D., 2003. Viewpoint: experimental recovery of geometrically necessary dislocation density in polycrystals. *Scr. Mater.* 48, 141–145.
- Field, D.P., Trivedi, P.B., Wright, S.I., Kumar, M., 2005. Analysis of local orientation gradients in deformed single crystals. *Ultramicroscopy* 103, 33–39.
- Fortier, P., Palumbo, G., Bruce, G.D., Miller, W.A., Aust, K.T., 1991. Triple line energy determination by scanning tunneling microscopy. *Scr. Metall. Mater.* 25, 177–182.
- Frank, F.C., 1950. The resultant content of dislocations in an arbitrary intercrystalline boundary. In: *Symposium on The Plastic Deformation of Crystalline Solids*, Mellon Institute, Pittsburgh, (NAVEXOS-P-834), vol. 150.
- Fressengeas, C., Taupin, V., Capolungo, L., 2011. An elasto-plastic theory of dislocation and disclination fields. *Int. J. Solids Struct.* 48, 3499–3509.
- Fressengeas, C., Taupin, V., Capolungo, L., Upadhyay, M., 2012. Tangential continuity of elastic/plastic curvature and strain at interfaces. *Int. J. Solids Struct.* 49, 2660–2667.
- Friedel, J., 1964. *Dislocations*. Pergamon, London.
- Gertsman, V.Yu., Nazarov, A.A., Romanov, A.E., Valiev, R.Z., Vladimirov, V.I., 1989. Disclination-structural unit model of grain boundaries. *Phil. Mag. A* 59, 1113.
- Hurtado, J.A., Elliott, B.R., Shodja, H.M., Gorelikov, D.V., Campbell, C.E., Lippard, H.E., Isabell, T.C., Weertmann, J., 1995. Disclination grain boundary model with plastic deformation by dislocations. *Mat. Sci. Eng. A* 190, 1.
- Kacher, J., Landon, C., Adams, B.L., Fullwood, D., 2009. Bragg's law diffraction simulations for electron backscatter diffraction analysis. *Ultramicroscopy* 109, 1148–1156.
- Kröner, E., 1958. Kontinuumstheorie der versetzungen und eigenspannungen. In: Collatz, L., Lösch, F. (Eds.), *Ergebnisse der Angewandte Mathematik*, vol. 5. Springer, Heidelberg, pp. 1–179.
- Kröner, E., 1980. Continuum theory of defects. In: Balian, R. et al. (Eds.), *Physics of Defects*. North Holland, Amsterdam, pp. 218–314.
- Li, J.C.M., 1972. Disclination model of high angle grain boundaries. *Surf. Sci.* 31, 12.
- Malhaire, C., Seguinéau, C., Ignat, M., Josserond, C., Debove, L., Brida, S., Desmares, J.M., 2009. Experimental setup and realization of thin film specimens for microtensile tests. *Rev. Sci. Instr.* 80 (023901), 1–5.
- Motylenko, M., Klemm, V., Klimanek, P., Pavlovitch, T., Straube, H., 2004. Characterization of the cell block structure and disclination configurations in plastically deformed metals by electron diffraction. *J. Alloy Compd.* 378, 93–96.
- Murayama, M., Howe, J.M., Hidaka, H., Takaki, S., 2002. Atomic-level observation of disclination dipoles in mechanically milled nanocrystalline Fe. *Science* 295, 2433.
- Nazarov, A.A., Bachurin, D.V., Shenderova, O.A., Brenner, D.W., 2003. On the origin and energy of triple junction defects due to the finite length of grain boundaries. *Interf. Sci.* 11, 417–424.
- Nye, J.F., 1953. Some geometrical relations in dislocated crystals. *Acta Metall.* 1, 153.
- Pantleon, W., 2008. Resolving the geometrically necessary dislocation content by conventional electron backscattering diffraction. *Scr. Mater.* 58, 994–997.
- Romanov, A.E., Vladimirov, V.I., 1992. Disclinations in crystalline solids. In: Nabarro, F.R.N. (Ed.), *Dislocations in Solids*, vol. 9. Elsevier, Amsterdam, p. 191.
- Romanov, A.E., Kolesnikova, A.L., 2009. Application of disclination concept to solid structures. *Prog. Mat. Sci.* 54, 740.
- Shih, K.K., Li, J.C.M., 1975. Energy of grain boundaries between cusp misorientations. *Surf. Sci.* 50, 109.
- Srinivasan, S.G., Cahn, J.W., Jónsson, H., Kalonji, G., 1999. Excess energy of grain-boundary triple junctions: an atomistic simulation study. *Acta Mater.* 47, 2821–2829.

- Tóth, L.S., Beausir, B., Gu, C., Estrin, Y., Scheerbaum, N., Davis, C.H.J., 2010. Effect of grain refinement by severe plastic deformation on the next-neighbor misorientation distribution. *Acta Mater.* 58, 6706–6716.
- Upadhyay, M., Capolungo, L., Taupin, V., Fressengeas, C., 2011. Grain boundary and triple line energies in crystalline media: a disclination based approach. *Int. J. Solids Struct.* 48, 3176–3193.
- Villert, S., Maurice, C., Wyon, X., Fortunier, R., 2009. Accuracy assessment of elastic strain measurement by EBSD. *J. Microsc.* 233, 290–301.
- Volterra, V., 1907. Sur l'équilibre des corps élastiques multiplement connexes. *Ann. Sci. Ecol. Norm. Sup.* III 24, 401–517.
- Wilkinson, A.J., Meaden, G., Dingley, D.J., 2006. High-resolution elastic strain measurement from electron backscatter diffraction patterns: new levels of sensitivity. *Ultramicroscopy* 106, 307–313.
- Zisman, A.A., Van Boxel, S., Seefeldt, M., Van Houtte, P., 2008. Gradient matrix method to image crystal curvature by processing of EBSD data and trial recognition of low-angle boundaries in IF steel. *Mater. Sci. Eng. A* 474, 165–172.